PHYSICAL REVIEW B **73**, 094104 (2006)

Channeling effects in high-angular-resolution electron spectroscopy

L. J. Allen,[1] S. D. Findlay,[1] M. P. Oxley,[2] C. Witte,[1] and N. J. Zaluzec[3]
[1]*School of Physics, University of Melbourne, Victoria 3010, Australia*
[2]*Condensed Matter Sciences Division, Oak Ridge National Laboratory, P. O. Box 2008, Oak Ridge, Tennessee 37831-6030, USA*
[3]*Electron Microscopy Center, Materials Science Division, Argonne National Laboratory, Argonne, Illinois 60439, USA*

(Received 21 September 2005; published 3 March 2006)

Momentum-transfer-resolved electron spectroscopy is a technique for examining the electronic structure of materials and requires the use of detectors accepting a small range of momentum transfers. For crystalline specimens, it is necessary to consider the channeling behavior of the fast electrons both before and after inelastic scattering to adequately describe the signals produced. Using oxygen *K*-shell core loss in NiO as a case study, we examine channeling in high-angular-resolution electron-channeling electron spectroscopy. The roles of nonlocality and sample thickness as they relate to the channeling effect are explored. Particular attention is given to the behavior arising from the channeling of the scattered electrons, as compared with models in which only the incident electrons channel. Calculations allowing for the channeling of both the incident and the scattered electrons are computationally demanding and we explore approximations that can be made for detectors with small acceptance angles.

DOI: 10.1103/PhysRevB.73.094104 PACS number(s): 61.14.Dc, 61.85.+p

I. INTRODUCTION

Momentum-transfer-resolved electron energy loss spectroscopy,[1,2] sometimes called q-resolved electron energy loss spectroscopy (EELS), is a useful method for investigating the electronic structure of materials. Attaining high angular resolution with this technique requires the use of a detector accepting a very limited range of momentum transfers. Given that the acceptance angles of detectors used in such experiments are often smaller than a Bragg angle,[1–12] it must be anticipated that the channeling, by which we mean the dynamical scattering, of the fast electron both before and after the energy loss event of interest will have a significant effect on the detected signal.

Simulations routinely incorporate the channeling of the incident electron. Many methods for the theoretical description of the channeling of the fast electrons both before and after inelastic scattering, sometimes called double-channeling methods, exist in the literature.[13–20] However, for inner-shell ionization, simulations incorporating the channeling of the scattered electrons are rare,[19,20] though for detectors with sufficiently small scattering angle the channeling of the scattered electrons is just as important as that of the incident electrons as we shall show. The approach here follows that of Josefsson and Allen,[20] using mixed dynamic form factors (MDFFs) for the treatment of inelastic scattering.[18–23] Because of the computational complexity involved in double-channeling calculations we shall describe the core-loss process using a hydrogenic model,[14,24–26] though more general models are possible.[16,27–30]

We shall take as a case study oxygen *K*-shell core-loss excitations in NiO as examined by high-angular-resolution electron-channeling electron spectroscopy (HARECES).[5,11] Since we are primarily interested in the channeling, we shall integrate over the fine structure in the experimental spectrum and compare with simulations which treat the ionization as if from an isolated atom. We shall summarize single-channeling theory by way of introduction to our explorations of the dynamics arising from double channeling and to highlight the importance of double channeling when detectors with small acceptance angles are used (previous demonstrations of double channeling were based on detector acceptance angles two orders of magnitude larger).[19] Our results confirm that such simulations, a useful adjunct to both experimental design and interpretation, must include double channeling for such small detector apertures and account correctly for the nonlocal nature of the effective interaction potential.[22,27,31] Double-channeling simulations require considerable computational effort and we explore some simplifying approximations.

II. THE EXPERIMENT

The experimental measurements in this work were recorded from a single-crystal specimen of NiO in a FEI Tecnai F20 ST field emission gun transmission and scanning transmission electron microscope (TEM-STEM) at Argonne National Laboratory (ANL). The NiO [001] specimen was cut from a large crystal grown at ANL and was prepared for TEM by careful mechanical dimpling, followed by conventional high- and low-energy argon ion milling to perforation. Prior to TEM measurements both the specimen and stage were plasma cleaned in an argon plasma for 15 min in a South Bay Technology plasma cleaner to mitigate the deleterious effects of specimen contamination,[32] the latter process being done to minimize the effects of any hydrocarbon contamination during the temporally extended measurement of approximately 12 h used to achieve statistically significant data. Conventional EELS and x-ray energy-dispersive spectroscopy measurements were also performed prior to HARECES measurements to confirm the nominal composition of the specimen and the absence of any major contaminants from the specimen preparation procedure.

During data acquisition, the microscope was operated at 200 keV with the incident probe adjusted to achieve nearly parallel illumination conditions. This was accomplished using the condenser-objective lens of the instrument, together with a nominal 50 μm second condenser aperture. Under these conditions a probe size on the sample of approximately 100 nm in diameter was defined. The region of interest (ROI) defined by this probe was chosen to be free of bend contours. However, due to the modest probe diameter and the sample preparation procedure employed, the analyzed region was not uniformly thick but had a wedged thickness profile. Using $\langle 200 \rangle$ extinction contours, the variation of thickness over the ROI was determined to range between 39 and 78 nm. Although more precise measurements of the thickness at any single point within the ROI using convergent-beam electron diffraction techniques was possible this was not deemed necessary since, as will be demonstrated later, the data analysis procedure results in an explicit determination of the thickness variation over the analyzed region.

The incident beam convergence semiangle was adjusted to $\leqslant 0.05$ mrad, and was set by controlling the illumination conditions of the condenser lens in the nanoprobe operating mode. The EELS detector, whose semiangle was 0.195 mrad, was centered on the forward direction in the symmetric orientation. The value of its collection semiangle was adjusted through the use of diffraction lens camera length and adjustable fixed apertures in front of the spectrometer. All measurements were performed with the instrument operating in the diffraction mode, with the EELS detector fixed relative to the crystal.

Excitation of the $\langle 200 \rangle$ systematic row was obtained by tilting the specimen away from the $[001]$ zone axis around the $\langle 200 \rangle$ direction by an angle of about 50 mrad using the goniometer stage of the microscope. To facilitate the precise control of the incident beam orientation, the probe was tilted, during measurements, by means of the microscope deflection coils using a custom computer program which is able to control both the instrument pre- and postspecimen deflection coils as well as the data acquisition system. Prior to any measurements, the beam tilt pivot points of the instrument were manually adjusted, to minimize any lens aberration induced probe motion. After these adjustments, it was possible to accurately tilt the incident probe in a two-dimensional raster pattern over the fixed region of interest on the specimen and simultaneously record electron energy loss spectra with minimal intervention. For the data reported herein, one-dimensional raster scans were performed along $\mathbf{G}=\langle 200 \rangle$ over the angular range of $\pm 1.5\mathbf{G}$. One hundred and fifty-one sequential spectra were recorded, giving an angular resolution of 0.25 mrad.

Figure 1(a) shows a typical electron energy loss spectrum with the beam in the symmetric position, while Fig. 1(b) shows, as a function of beam orientation, the variation in the background-corrected integrated intensity for a 100 eV energy window above the oxygen K-shell ionization threshold. This integration averages out the near-edge structure above threshold, enabling comparisons with simulations which do not include this fine structure. The background subtraction was performed using the standard power-law model using a 50 eV window before the oxygen K-shell edge.[33] Figure 1(c) presents a two-dimensional plot of the complete data set illustrating the complex variation of the near-edge fine structure of the oxygen K-shell spectra as a function of orientation.

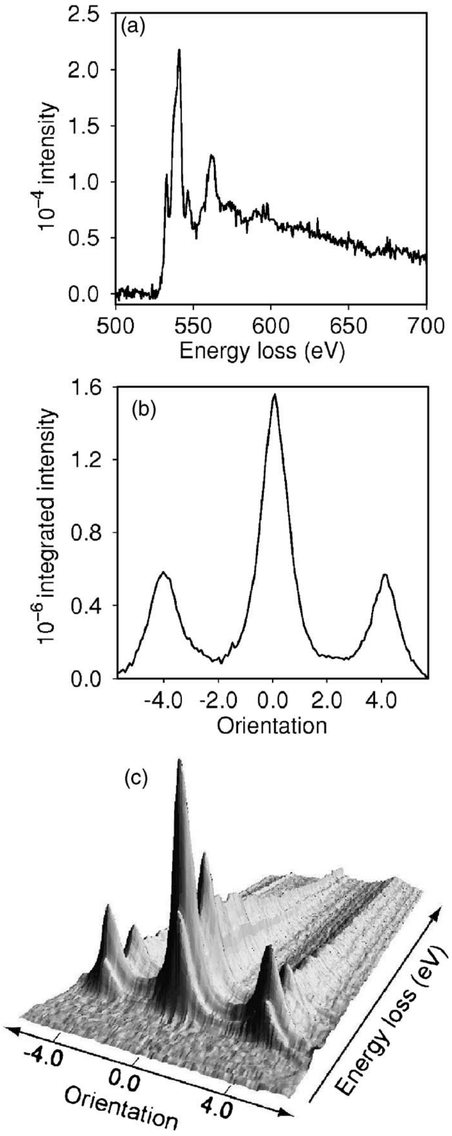

FIG. 1. (a) Oxygen K-shell energy loss spectrum from NiO in the symmetric orientation of the $\langle 200 \rangle$ systematic row. (b) Integrated intensity over a 100 eV energy window above ionization threshold. Background subtraction was carried out based on extrapolation from a 50 eV window prior to the edge. A unit of 1.0 on the orientation axis puts the (100) beam in the exact Bragg orientation, a tilt of 3.0 mrad. (c) Surface plot of the orientation dependence of the background-corrected oxygen K-shell EELS structure as a function of energy loss.

III. THE POTENTIAL, NONLOCALITY AND THE BRAGG PEAKS

Assuming an incident plane wave, the cross section for inelastic scattering from an isolated atom, or from a crystal when elastic scattering prior to inelastic scattering is ignored, is determined by the dynamic form factor.[18,21,34] For a fixed detector geometry the dynamic form factor may be regarded as a function of the incident beam direction $\mathbf{K}$ (magnitude K) and energy loss ϵ: $S(\mathbf{K},\epsilon)$. For a detector with small entrance aperture we expect the cross section for an isolated atom to drop off as the incident beam is tilted away from the detector.

If the presence of the crystal did not significantly alter the wave function of the incident electrons then the cross section from the crystal would also drop off smoothly. The presence of the Bragg peaks in the experimental signal in Fig. 1(b) is therefore direct evidence that scattering of the wave function within the crystal is significant, that channeling is important.

Channeling or scattering within the crystal prior to the energy loss event of interest means that the wave causing the ionization is not a single plane wave but a superposition of many. The necessary and sufficient information to completely specify the inelastic scattering in such a case is given by the so-called *mixed* dynamic form factor.[18] It may be expressed as $S(\mathbf{K},\tilde{\mathbf{K}},\epsilon)$, and describes the contribution to the cross section from the interference between incident plane waves with wave vectors $\mathbf{K}$ and $\tilde{\mathbf{K}}$.[21,23] Before considering the theory for describing the channeling, it is worth reviewing some features of the MDFFs, or rather the inelastic scattering coefficients that depend on them.

A plane wave with wave vector $\mathbf{K}$ incident upon a crystalline specimen will, through Bragg diffraction, excite a set of plane waves with wave vectors of the form $\mathbf{K}+\mathbf{G}$. (The capital notation for the reciprocal lattice vectors $\mathbf{G}$ and $\mathbf{H}$ is used when the mesh is related to the reciprocal lattice of the crystal. Lower-case $\mathbf{g}$ and $\mathbf{h}$ will be used when a finer mesh is required.) The interference terms produced can thus be defined simply by the components $\mathbf{G}$ and $\mathbf{H}$ involved. The inelastic scattering coefficients are obtained from the MDFFs by extracting just that portion corresponding to a particular type of energy loss event, inner-shell ionization say, folding in details of the detector through an integration over acceptance angle and an energy loss window (which implicity assumes a single-channeling approximation), and summing over the detected final states.[22] For inner-shell ionization, these inelastic scattering coefficients may be written as[27,28,35]

$$\mu_{\mathbf{H},\mathbf{G}}(\mathbf{K}) = \frac{1}{2\pi K V_c}\sum_n \exp[-M_n(\mathbf{G}-\mathbf{H})] \times \exp[2\pi i(\mathbf{G}-\mathbf{H})\cdot\boldsymbol{\tau}_n] f_{\mathbf{H},\mathbf{G}}(\mathbf{K}). \tag{1}$$

The sum over n includes only those atoms of the species being ionized, with site $\boldsymbol{\tau}_n$ and Debye-Waller factor $M_n(\mathbf{G}) = 2\pi^2\langle u_n^2\rangle G^2$, where $\langle u_n^2\rangle$ is the projected mean square thermal displacement, in the unit cell of volume V_c. The atomic scattering factors are given by

$$f_{\mathbf{H},\mathbf{G}}(\mathbf{K}) = \frac{1}{2\pi^3 a_0^2}\int K'\kappa^2\left[\int\left(\sum_{m_l} n_{m_l}\frac{\int F^*_{l,m_l}(\mathbf{q}+\mathbf{H},\boldsymbol{\kappa})F_{l,m_l}(\mathbf{q}+\mathbf{G},\boldsymbol{\kappa})d\Omega_\kappa}{|\mathbf{q}+\mathbf{H}|^2|\mathbf{q}+\mathbf{G}|^2}\right)d\Omega_{K'}\right]d\kappa, \tag{2}$$

where a_0 is the relativistic Bohr radius and K' is the magnitude of the wave vector $\mathbf{K}'$ of the scattered electron. The wave vector of the ejected electron is denoted by $\boldsymbol{\kappa}$ (magnitude κ). The scattering vector $\mathbf{q}=\mathbf{K}-\mathbf{K}'$. The range of the angular integration, $d\Omega_{K'}$, is determined by the geometry of the detector. The energy window of the detector defines the range of the κ integration. The atomic transition matrix element is given by

$$F_{l,m_l}(\mathbf{q}+\mathbf{H},\boldsymbol{\kappa}) = \int u^*(\boldsymbol{\kappa},\mathbf{r})\exp[2\pi i(\mathbf{q}+\mathbf{H})\cdot\mathbf{r}]u_{l,m_l}(\mathbf{r})d\mathbf{r}, \tag{3}$$

where $u_{l,m_l}(\mathbf{r})$ and $u(\boldsymbol{\kappa},\mathbf{r})$ are the wave functions of the (appropriately normalized) bound and continuum states, respectively. The matrix elements are for a specific suborbital in an atom, defined by the orbital angular momentum l and the azimuthal quantum number m_l. Equation (2) sums over the possible values of the azimuthal quantum number m_l, and the factor n_{m_l} accounts for the number of electrons in each suborbital. The MDFF is essentially the numerator in Eq. (2).

The above formulation is general, but we shall utilize the hydrogenic model for the bound and continuum states, restricting our consideration to K-shell core loss. Much of Eq. (2) may then be evaluated analytically,[14,24–26] which helps make the computationally demanding double-channeling calculations more tractable.

Following Oxley *et al.*,[31] a (projected) real space form for the effective scattering potential may be defined via

$$W(\mathbf{r}_\perp,\mathbf{r}'_\perp) = \frac{h^2 K}{2\pi m V}\sum_{\mathbf{h},\mathbf{g}}\mu_{\mathbf{h},\mathbf{g}}e^{2\pi i\mathbf{h}\cdot\mathbf{r}_\perp}e^{-2\pi i\mathbf{g}\cdot\mathbf{r}'_\perp}, \tag{4}$$

where V denotes the crystal volume. The consequence of the interference terms is to produce an effective potential which is a function of two two-dimensional vectors: a nonlocal potential. As the cross section will be formulated, for a given incident orientation $\mathbf{K}$ one need only consider the inelastic scattering coefficients $\mu_{\mathbf{H},\mathbf{G}}(\mathbf{K})$ for which $\mathbf{G}$ and $\mathbf{H}$ are physical reciprocal lattice vectors. However, to plot the potential it is more convenient to use a supercell [hence the finer mesh of reciprocal lattice vectors $\mathbf{g}$ and $\mathbf{h}$ in Eq. (4)], as it gives a better feel for the nonlocality of the potential. Equation (4) is effectively four dimensional and is difficult to visualize. But in the systematic row case Eq. (4) reduces to a two-dimensional form $W(x,x')$ which can be plotted.

Figure 2(a) shows the effective scattering potential for oxygen K-shell ionization with $\mathbf{K}_\perp=\mathbf{0}$ assuming the detector geometry described in Sec. II. A 5×5 supercell was used for

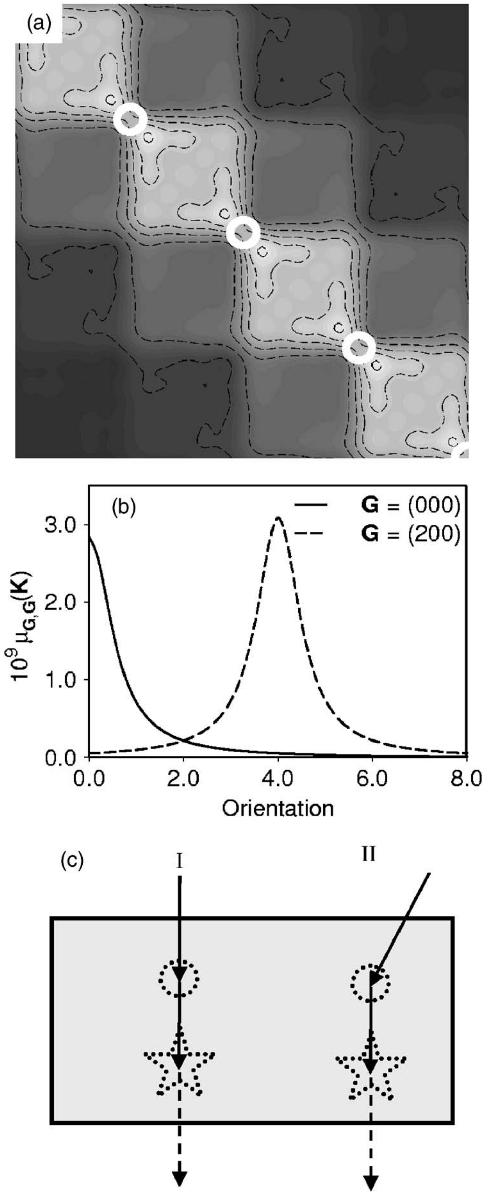

FIG. 2. (a) Effective ionization potential $W(x,x')$ for $\mathbf{K}_\perp=\mathbf{0}$ shown on a 2×2 supercell. The location of the oxygen atoms on the diagonal is shown by white rings. (b) Inelastic scattering coefficients $\mu_{\mathbf{G},\mathbf{G}}(\mathbf{K})$ as a function of $\mathbf{K}_\perp$ [$\mathbf{K}_\perp=-\text{orientation}\times(100)/2$], for $\mathbf{G}=(000)$ and (200). (c) Schematic of the primary scattering mechanism contributing to the detected signal for (I) $\mathbf{K}_\perp=\mathbf{0}$ and (II) $\mathbf{K}_\perp=\mathbf{G}$. The dotted circles denote elastic scattering, the dotted stars inelastic scattering.

sampling purposes, but only a 2×2 portion is shown. The projected locations of the oxygen atoms are denoted by white rings. Should the scattering be such that $\mu_{\mathbf{h},\mathbf{g}}\approx\mu_{\mathbf{h}-\mathbf{g},\mathbf{0}}$, implying $W(x,x')\approx V(x)\delta(x-x')$, which is to say $W(x,x')$ would fall off strongly away from the $x=x'$ diagonal, the potential would be local. It is evident in Fig. 2(a) that the potential spreads significantly off the diagonal: the effective interaction is highly nonlocal.

Figure 2(b) shows the magnitude of the inelastic scattering coefficient $\mu_{\mathbf{G},\mathbf{G}}(\mathbf{K})$ as a function of $\mathbf{K}_\perp$ for the cases $\mathbf{G}=(000)$ and $\mathbf{G}=(200)$. In both cases the inelastic scattering coefficients are a maximum for $\mathbf{K}_\perp=-\mathbf{G}$. The former corresponds to the orientation of the central peak in Fig. 1(b), the latter to the orientation of a Bragg peak. Note the angular width of these peaks. With a full width at half maximum of around 3.4 mrad, they are broader than the detector, smaller than a Bragg angle, and in good agreement with the characteristic scattering angle for this energy loss (532 eV).[36]

More importantly though, these plots suggest what inspection of all the matrix elements shows to be true: for $\mathbf{K}_\perp\approx-\mathbf{G}$ for the two $\mathbf{G}$ values under consideration, the magnitude of the matrix element $\mu_{\mathbf{G},\mathbf{G}}(\mathbf{K})$ is much larger than all others $\mu_{\mathbf{H},\mathbf{H}'}(\mathbf{K})$. Therefore we expect most of the contribution to the signal to come from the self-interference of the beam with orientation $\mathbf{K}+\mathbf{G}$. The physical interpretation follows readily. For the case $\mathbf{K}_\perp=\mathbf{G}=(000)$, $\mu_{\mathbf{G},\mathbf{G}}(\mathbf{K})$ describes the probability of inelastic scattering from the forward direction, and the contribution from each depth depends simply on the density of electrons in the $\mathbf{G}=(000)$ beam at that depth. This is shown schematically as process I in Fig. 2(c). For the case $\mathbf{K}_\perp=-\mathbf{G}=(\bar{2}00)$, $\mu_{\mathbf{G},\mathbf{G}}(\mathbf{K})$ describes the probability of inelastic scattering from the direction $\mathbf{G}$ relative to the beam, which, given $\mathbf{K}_\perp=-\mathbf{G}$, corresponds again to the forward direction within the crystal. The contribution from each depth then depends simply on the density of electrons in the (200) component at that depth, i.e., the portion which has through elastic scattering found itself traveling along the crystal normal direction. This is shown schematically as process II in Fig. 2(c).

The finite width of the peaks in Fig. 2(b) means that the "Bragg peak" need not have its maximum at precisely $\mathbf{K}_\perp=-\mathbf{G}$. If the proportion of the electron density in beam $\mathbf{G}$ increases faster than $\mu_{\mathbf{G},\mathbf{G}}(\mathbf{K})$ decreases for tilts away from $\mathbf{K}_\perp=-\mathbf{G}$ then the peak may be somewhat displaced.

IV. SINGLE CHANNELING

In examining the inelastic scattering coefficient for the chosen detector geometry we found that, for inclined illumination, obtaining a significant inelastic signal required a component to be scattered into the forward direction; process II in Fig. 2(c) requires an elastic scattering event prior to the ionization event. This section will focus on techniques for the inclusion of channeling prior to the ionization event.

The elastic wave function inside the crystal may be written in Bloch state form as

$$\psi_{\mathbf{K}}(\mathbf{r}_\perp,z)=\sum_i [C^{-1}(\mathbf{K})]_i^{\mathbf{0}} e^{2\pi i\lambda^i(\mathbf{K})z}\sum_{\mathbf{G}} C^i_{\mathbf{G}}(\mathbf{K})e^{2\pi i\mathbf{G}\cdot\mathbf{r}_\perp}, \quad (5)$$

where $\lambda^i=\gamma^i+i\eta^i$ are Bloch state eigenvalues, with γ^i the *anpassung* and η^i the absorption coefficients, and $C^i_{\mathbf{G}}$ are Bloch state eigenvector Fourier coefficients, all of which depend on the incident wave vector $\mathbf{K}$. We choose a real space coordinate system such that z increases into the crystal while $\mathbf{r}_\perp$ denotes the position parallel to the crystal surface. The notation for the excitation amplitude $[C^{-1}]_i^{\mathbf{0}}$, denoting an element from the inverse of the eigenvector matrix, has been chosen to clearly label the Bloch state and Fourier coefficient involved. A phase factor $e^{2\pi i\mathbf{K}\cdot\mathbf{r}}$ has been omitted to simplify notation and has no consequences for the theoretical development.

Using this elastic wave function in the single-channeling approximation the cross-section expression, as a function of sample thickness t and the incident beam orientation defined by the wave vector $\mathbf{K}$, may be written as[22]

$$\sigma(\mathbf{K},t) = NV_c \sum_{i,j} [C^{-1}(\mathbf{K})]_i^{\mathbf{0}} [C^{-1}(\mathbf{K})]_j^{\mathbf{0}*} L^{ij}(\mathbf{K},t) \times \sum_{\mathbf{G},\mathbf{H}} C_{\mathbf{G}}^{i}(\mathbf{K}) C_{\mathbf{H}}^{j*}(\mathbf{K}) \mu_{\mathbf{H},\mathbf{G}}(\mathbf{K}), \tag{6}$$

where

$$L^{ij}(\mathbf{K},t) = \frac{\exp\{2\pi i[\lambda^i(\mathbf{K}) - \lambda^{j*}(\mathbf{K})]t\} - 1}{2\pi i[\lambda^i(\mathbf{K}) - \lambda^{j*}(\mathbf{K})]t} \tag{7}$$

and NV_c is the illuminated volume (N unit cells each of volume V_c).

Allen and Josefsson presented a two-term cross-section expression.[22] They called the term given in Eq. (6) the dynamical term, the signal from electrons scattered directly out of the elastic beams by the scattering mechanism to which the inelastic scattering coefficients correspond. Their other term, the so-called diffuse term, models the signal from a diffuse background of electrons which undergo inelastic thermal scattering prior to the inelastic scattering from which the cross section derives. However, because of the added computational requirements, and because the generalization to the double-channeling regime is less clear, we shall neglect any diffuse term in this work, assuming a single elastic-to-inelastic transition approximation.[37] Note though that calculation of the elastic wave function appearing in Eq. (6) includes absorption due to thermal scattering: the proportion of electrons in the elastic wave function attenuates with increasing depth into the crystal.

Figure 3(a) shows the oxygen K-shell cross section as a function of orientation and thickness. The probe and detector parameters are those characterizing the experiment, save that the small convergence semiangle of the incident beam is neglected. The calculation is carried out for the ⟨200⟩ systematic row, which is to say that the only reciprocal lattice vectors included are multiples of (200), and the beam is rocked along the systematic row direction. In this and all further calculations seven Bragg beams are used and this number is sufficient for converged calculations. An orientation value of unity indicates that (100) is in the exact Bragg orientation. We shall label the tangential component of the incident wave vector relative to the symmetric position. Thus at the principal orientation, that of the central peak in Fig. 1(b), we write $\mathbf{K}_\perp = (000)$. The secondary peaks, which we simply call the Bragg peaks, correspond to $\mathbf{K}_\perp = \pm(200)$. Note that the (100) beam is forbidden in NiO.

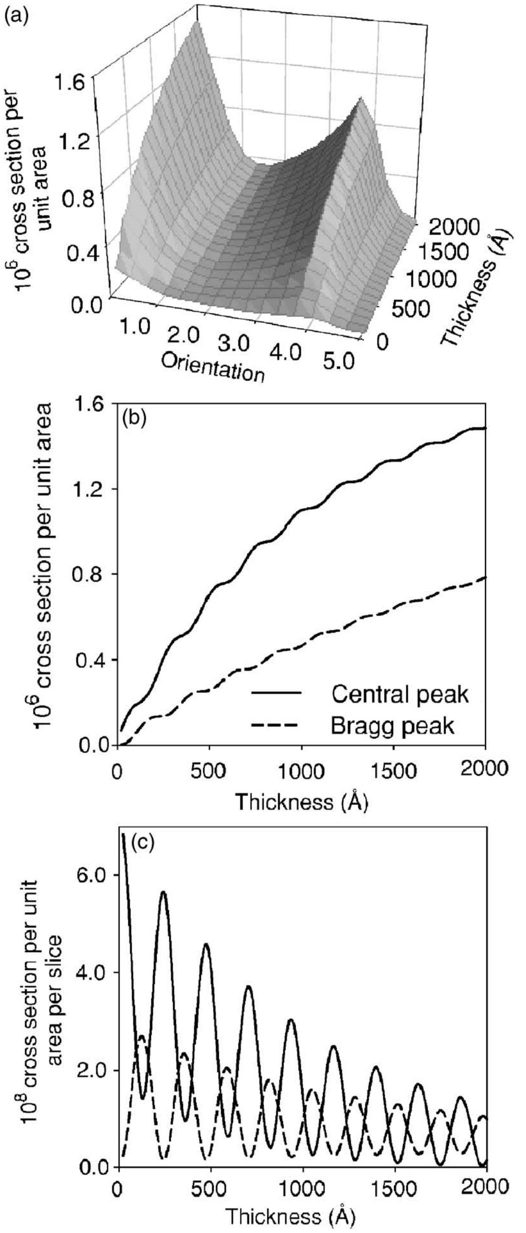

FIG. 3. (a) The cross section per unit area as a function of orientation and thickness in the single-channeling model. (b) The cross section per unit area as a function of thickness at orientations corresponding to the central and Bragg peaks. (c) The contribution per 25 Å thick slice to the signal plotted in (b).

Let us further examine the dynamical component at the symmetric and Bragg peak orientations. Figure 3(b) shows the variation of the cross section as a function of thickness for both the central peak (solid line) and the Bragg peak (dashed line). The Bragg peak plots were taken from the exact $\mathbf{K}_\perp = -\mathbf{G}$ orientation. But the Bragg peak, which from Fig. 3(a) is clearly asymmetric, has a maximum that is displaced inward somewhat by the mechanism discussed in the previous section. While both cross sections increase monotonically, slight oscillations can be seen. This is brought out in Fig. 3(c) where the cross section contribution "per slice" is shown as a function of thickness. The contribution per slice oscillates rapidly as a function of thickness at both the central peak and the Bragg peak. Note that the peaks of these two plots are out of step.

To better appreciate why we may consider a contribution per slice, we reexpress the cross-section expression, Eq. (6), in terms of wave functions[38]

$$\sigma(\mathbf{K},t) = NV_c \sum_{\mathbf{G},\mathbf{H}} \frac{1}{t}\int_0^t \Psi_{\mathbf{K}}(\mathbf{G},z)\Psi^*_{\mathbf{K}}(\mathbf{H},z)dz\,\mu_{\mathbf{H},\mathbf{G}}(\mathbf{K}), \tag{8}$$

where the two-dimensional Fourier transform of the wave function is given by

$$\Psi_{\mathbf{K}}(\mathbf{G},z) = \frac{1}{A}\int_A \psi_{\mathbf{K}}(\mathbf{r}_\perp,z)e^{-2\pi i\mathbf{G}\cdot\mathbf{r}_\perp}d\mathbf{r}_\perp. \tag{9}$$

Equation (8) consists of an integral over z of positive definite terms, an incoherent sum over contributions from different depths. This enables us to meaningfully consider contributions per slice in Fig. 3(c).

A further useful variant on Eq. (6) uses scattering matrices:

$$\sigma(\mathbf{K},t) = NV_c \sum_{\mathbf{G},\mathbf{H}} \frac{1}{t}\int_0^t \mathcal{S}_{\mathbf{G},\mathbf{0}}(\mathbf{K},z)\mathcal{S}^*_{\mathbf{H},\mathbf{0}}(\mathbf{K},z)dz\,\mu_{\mathbf{H},\mathbf{G}}(\mathbf{K}), \tag{10}$$

where the scattering matrix elements are defined by

$$\mathcal{S}_{\mathbf{G},\mathbf{H}}(\mathbf{K},z) = \sum_i [C^{-1}(\mathbf{K})]_i^{\mathbf{H}} e^{2\pi i\lambda^i(\mathbf{K})z} C^i_{\mathbf{G}}(\mathbf{K}), \tag{11}$$

and may be interpreted as transition matrix elements for elastic scattering between plane wave components $\mathbf{K}+\mathbf{H}$ and $\mathbf{K}+\mathbf{G}$ over a thickness z.

V. DOUBLE CHANNELING

The single-channeling approximation assumes that the inelastically scattered electrons can be modeled as plane waves. This never describes the true scattering; the propagation of the inelastically scattered electrons should be described via Bloch states as is done for the elastically scattered electrons. It has been demonstrated that the single-channeling model adequately approximates the total signal when the detector is large,[20] because a large detector aperture integrates over the detailed distribution of the scattered electrons. For the small detector aperture used in the experiment in Sec. II we anticipate the single-channeling model to be a poor approximation. Therefore, having discussed the simpler model by way of introduction, let us now explore the full double-channeling model.

A. Theory

When the scattered electrons are treated as Bloch waves, the more realistic treatment, a double-channeling formulation is obtained. Following Josefsson and Allen[20] the cross section may be written as

$$\begin{aligned}\sigma(\mathbf{K},t) = {}& NV_c\frac{2m}{\hbar^2 K}\sum_{i,j}[C^{-1}(\mathbf{K})]_i^{\mathbf{0}}[C^{-1}(\mathbf{K})]_j^{\mathbf{0}*}\sum_{\mathbf{H},\mathbf{G}} C^i_{\mathbf{G}}(\mathbf{K})C^{j*}_{\mathbf{H}}(\mathbf{K})\sum_{p\neq 0}\int\sum_{i',j'} C^{j'*}_{\mathbf{0}}(\mathbf{K}')C^{i'}_{\mathbf{0}}(\mathbf{K}')L^{iji'j'}(\mathbf{K},\mathbf{K}',t)\\ &\times\sum_{\mathbf{H}',\mathbf{G}'}[C^{-1}(\mathbf{K}')]_{i'}^{\mathbf{G}'}[C^{-1}(\mathbf{K}')]_{j'}^{\mathbf{H}'*}\frac{K'}{2}X^p_{\mathbf{H}-\mathbf{H}',\mathbf{G}-\mathbf{G}'}(\mathbf{K},\mathbf{K}')d\Omega_{K'}.\end{aligned} \tag{12}$$

where

$$X^p_{\mathbf{H}-\mathbf{H}',\mathbf{G}-\mathbf{G}'}(\mathbf{K},\mathbf{K}') = \mathcal{F}_{\text{site}}\frac{4\hbar^2}{ma_0^2}\frac{1}{V}\frac{F^*_{l,m_l}(\mathbf{q}+\mathbf{H}-\mathbf{H}',\boldsymbol{\kappa}_p)}{4\pi^2|\mathbf{q}+\mathbf{H}-\mathbf{H}'|^2}\frac{F_{l,m_l}(\mathbf{q}+\mathbf{G}-\mathbf{G}',\boldsymbol{\kappa}_p)}{4\pi^2|\mathbf{q}+\mathbf{G}-\mathbf{G}'|^2}, \tag{13}$$

$$\mathcal{F}_{\text{site}} = \sum_n e^{-M_n(\mathbf{G}-\mathbf{G}'-\mathbf{H}+\mathbf{H}')}e^{2\pi i(\mathbf{G}-\mathbf{G}'-\mathbf{H}+\mathbf{H}')\cdot\boldsymbol{\tau}_n}, \tag{14}$$

$$L^{iji'j'}(\mathbf{K},\mathbf{K}',t) = \frac{\exp\{2\pi i[\lambda^i(\mathbf{K})-\lambda^{j*}(\mathbf{K})]t\} - \exp\{2\pi i[\lambda^{i'}(\mathbf{K}')-\lambda^{j'*}(\mathbf{K}')]t\}}{2\pi i[\lambda^i(\mathbf{K})-\lambda^{j*}(\mathbf{K})-\lambda^{i'}(\mathbf{K}')+\lambda^{j'*}(\mathbf{K}')]t}. \tag{15}$$

Here the sum over final states p is written in discrete form, but for ionization will become an integral over the continuum of energy loss values consistent with the energy window of the detector. There are small differences between Eqs. (12)–(15) and the corresponding expression in Josefson and Allen,[20] where the boundary condition on the exit surface was assumed to be different, but Eqs. (12)–(15) are in keeping with the earlier work of Allen.[39]

The above expression for the cross section may be recast in terms of scattering matrices as

$$\sigma(\mathbf{K},\mathbf{K}',t) = NV_c\frac{2m}{\hbar^2 K}\sum_{p\neq 0}\int \sum_{\mathbf{H},\mathbf{G},\mathbf{H}',\mathbf{G}'}\frac{1}{t}\int_0^t \mathcal{S}_{\mathbf{G},\mathbf{0}}(\mathbf{K},z)\mathcal{S}^*_{\mathbf{H},\mathbf{0}}(\mathbf{K},z)\mathcal{S}_{\mathbf{0},\mathbf{G}'}(\mathbf{K}',t-z)\mathcal{S}^*_{\mathbf{0},\mathbf{H}'}(\mathbf{K}',t-z)dz\frac{K'}{2}X^p_{\mathbf{H}-\mathbf{H}',\mathbf{G}-\mathbf{G}'}(\mathbf{K},\mathbf{K}')d\Omega_{K'}, \tag{16}$$

which can be interpreted as follows: $\mathcal{S}_{\mathbf{G},\mathbf{0}}(\mathbf{K},z)$ gives the probability of elastic scattering from $\mathbf{K}+\mathbf{0}$ to $\mathbf{K}+\mathbf{G}$ through a thickness z of sample, including absorptive effects; $\mathcal{S}_{\mathbf{0},\mathbf{G}'}(\mathbf{K}',t-z)$ describes the probability of elastic scattering from $\mathbf{K}'+\mathbf{G}'$ to $\mathbf{K}'+\mathbf{0}$ by a thickness $t-z$ of sample; and the inelastic matrix element, involving $\mathbf{G}-\mathbf{G}'$, joins these processes. A similar thing happens with the complex conjugate terms. Together the expression embodies the contribution from all elastic scattering to the depth z, undergoing inelastic transition, and elastic scattering to the direction $\mathbf{K}'$ within the detector (the integral over $d\Omega_{K'}$ being over all angles accepted by the detector).

Figure 4(a) shows the dynamical contribution to the oxygen K-shell cross section as a function of thickness and orientation, which should be compared with the single-channeling result in Fig. 3(a). Rather than the contributions to the central and Bragg peaks increasing monotonically as they did in the single channeling case, these intensities oscillate with increasing sample thickness. Additionally, the displacement of the Bragg peak maximum from the exact $\mathbf{K}_\perp = -\mathbf{G}$ orientation shifts back and forth with varying thickness. Figure 4(b) plots the intensities at the two orientations. This shows not only how pronounced the oscillations are, but further that they are again out of step [cf. the single-channeling per slice contributions in Fig. 3(c)], such that there are thicknesses at which the signal on the Bragg peak exceeds that on the central peak. A simple qualitative explanation can be given for this oscillatory behavior, but we shall defer it to discuss some simplifying assumptions which will enable us to better illustrate how the oscillatory behavior comes about.

B. Simplifying assumptions

The qualitative differences between the double-channeling and the single-channeling results demonstrate the need for the double-channeling model when detectors with such small apertures are used. However the double-channeling approach is computationally demanding. The single-channeling expression scales as N^4 while the double-channeling expression scales as N^8, where N is the number of beams used in the Bloch state calculation and the scaling follows directly from the number of summations involved in Eqs. (6) and (12).[20] This was a strong motivating factor in selecting a systematic row condition rather than a zone axis orientation, since a smaller number of beams suffices. Furthermore the final Bloch state, depending on $\mathbf{K}'$, is recalculated for each direction used in the evaluation of the integral over the detector semiangle and for each energy loss in the evaluation of the integral over the detector energy window. However, some simplifications are possible.

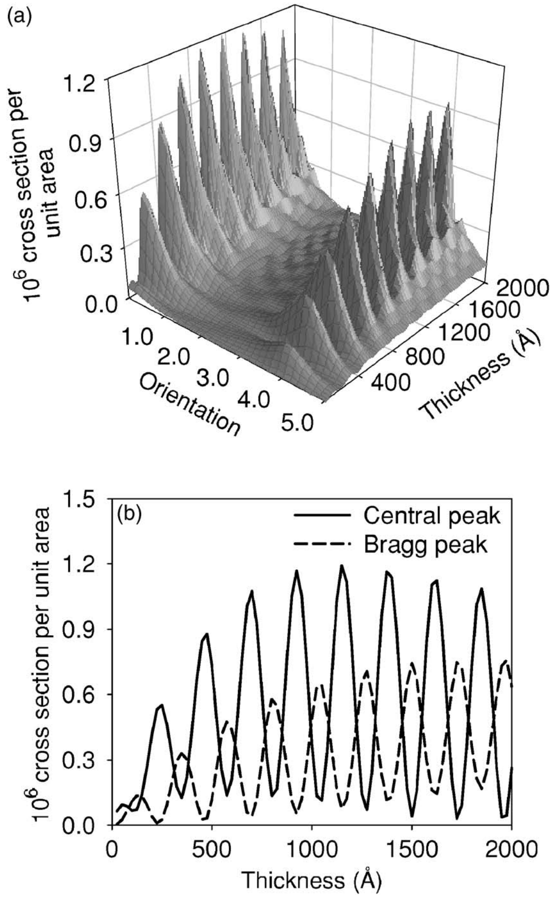

FIG. 4. (a) The cross section per unit area as a function of orientation and thickness in the double-channeling model. (b) Extracts from (a) at the central and Bragg peaks.

Rather than discussing the detailed Bloch form, we shall make approximations on the scattering matrix form of Eq. (16) for simplicity of notation. The dependence of the scattering matrix on energy is weak on the scale of the 100 eV detector energy window. Let us therefore take a single representative value of K', say the incident beam energy less the ionization threshold, and move the scattering matrices outside the sum over the final state energy. Moreover the detector aperture is so small that the scattering matrix dependence on the direction of $\mathbf{K}'$ is weak within the detector. We therefore take a representative value for the direction of $\mathbf{K}'$, and reduce the integration over the detector semiangle to a product of the integrand with the detector solid angle. Equation (16) then simplifies to

$$\sigma(\mathbf{K},\mathbf{K}',t) = NV_c \sum_{\mathbf{H},\mathbf{G},\mathbf{H}',\mathbf{G}'} \frac{1}{t}\int_0^t \mathcal{S}_{\mathbf{G},\mathbf{0}}(\mathbf{K},z)\mathcal{S}^*_{\mathbf{H},\mathbf{0}}(\mathbf{K},z)\mathcal{S}_{\mathbf{0},\mathbf{G}'}(\mathbf{K}',t-z)\mathcal{S}^*_{\mathbf{0},\mathbf{H}'}(\mathbf{K}',t-z)\,dz\,\mu_{\mathbf{H}-\mathbf{H}',\mathbf{G}-\mathbf{G}'}(\mathbf{K},\mathbf{K}'), \tag{17}$$

where

$$\mu_{\mathbf{H}-\mathbf{H}',\mathbf{G}-\mathbf{G}'}(\mathbf{K},\mathbf{K}') = \frac{2m}{\hbar^2 K}\sum_{p\neq 0}\frac{K'}{2}X^p_{\mathbf{H}-\mathbf{H}',\mathbf{G}-\mathbf{G}'}(\mathbf{K},\mathbf{K}')\Delta\Omega_{K'}, \tag{18}$$

in which $\Delta\Omega_{K'}$ is the solid angle subtended by the detector. Careful comparison of the content of Eqs. (13) and (18) with that of Eqs. (1) and (2) draws out the similarity that has motivated us to revert to a μ-matrix element notation. For the small detector used, signals calculated in this way differ imperceptibly from those given in Fig. 4(b).

Equation (17) offers some insight into the oscillatory features in Fig. 4. Compare Eq. (17) with the dynamical term in the single-channeling result of Eq. (10): the scattering matrices for the incident wave are unchanged, but Eq. (17) includes two further scattering matrices describing the scattered electron. Moreover, the additional matrices depend not only on the depth of ionization but also on the total specimen thickness t.

The integrand in the single-channeling case, Eq. (10), is positive definite. As a result the total signal derives from the incoherent sum of the contributions from all depths within the sample. This is evident in Fig. 3 where the signal grows monotonically with increasing thickness, since the signal arising from a crystal of thickness $t+\delta t$ is simply the sum of that deriving from a crystal of thickness t plus the (positive) contribution from the final portion of thickness δt. This enabled us to plot a per slice contribution as the difference in total cross section between crystals of different thicknesses. But in the double-channeling case the integrand in Eq. (17) is also positive definite and the contributions from each depth add incoherently. How then does the oscillatory behavior arise?

The difference between the two cases, which allows for oscillatory behavior in the double-channeling treatment, is that the integrand in Eq. (17) depends not only on the depth z but also on the total crystal thickness t. Thus while for a given thickness t the total signal derives from an incoherent sum over the individual slices, the evaluation for a different thickness $t+\delta t$ is not simply a matter of adding a further contribution from the δt layer. Rather the entire sum needs to be reevaluated because the contribution from each depth will change due to the new total thickness. The thickness dependence of the integrand is present only in the scattering matrices for the channeling subsequent to energy loss, and as such the difference expresses the physical property that the signal detected from ionization of some atom at a particular depth will depend on thickness of crystal remaining: channeling through the remaining portion affects the probability of the scattered electron reaching the detector.

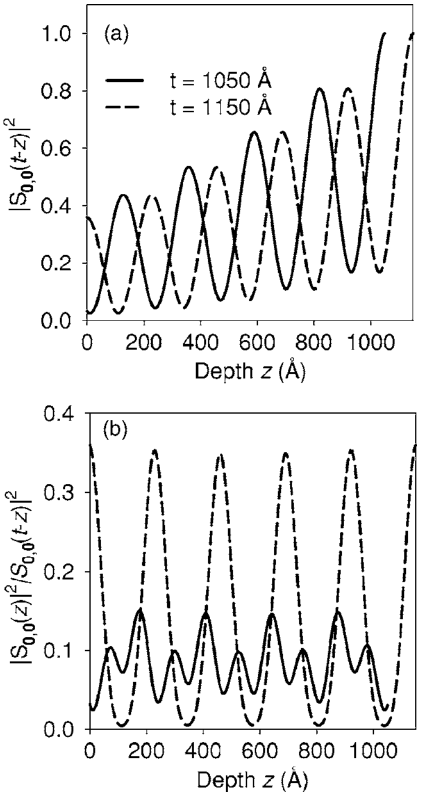

FIG. 5. (a) $|\mathcal{S}_{\mathbf{0},\mathbf{0}}(\mathbf{K}_\perp=\mathbf{0},t-z)|^2$ as a function of the event depth z for $t=1050$ and 1150 Å. (b) $|\mathcal{S}_{\mathbf{0},\mathbf{0}}(\mathbf{K}_\perp=\mathbf{0},z)|^2|\mathcal{S}_{\mathbf{0},\mathbf{0}}(\mathbf{K}_\perp=\mathbf{0},t-z)|^2$ as a function of event depth z. The total cross section consists of the sum of integrals over z of such products weighted by the inelastic scattering coefficients.

Let us take an example to get a better feel for how this comes about. We shall consider the symmetric orientation $\mathbf{K}_\perp=\mathbf{0}$. The inelastic scattering coefficients in Eq. (18) are now essentially those of Eq. (1). In particular it is still true that at this orientation $\mu_{\mathbf{0},\mathbf{0}}$ is significantly larger than all other $\mu_{\mathbf{H},\mathbf{G}}$. In the single-channeling expression of Eq. (10), this restriction reduced the sum to a single term: $|\mathcal{S}_{\mathbf{0},\mathbf{0}}(\mathbf{K},z)|^2$. However, in the double-channeling expression of Eq. (17) this restriction only allows us to collapse two of the four sums by forcing $\mathbf{G}'=\mathbf{G}$ and $\mathbf{H}'=\mathbf{H}$. To demonstrate the idea we shall consider only the single case $\mathbf{G}'=\mathbf{H}'=\mathbf{0}$ from this sum; other terms will be important, but this term will serve our illustration. Figure 5(a) plots $|\mathcal{S}_{\mathbf{0},\mathbf{0}}(\mathbf{K}_\perp=\mathbf{0},t-z)|^2$, the scattering matrix contributions from the scattered electron with $\mathbf{G}'=\mathbf{H}'=0$ in Eq. (17), for $t=1050$ and 1150 Å. These thickness values were chosen because they correspond to an adjacent minimum and maximum in the oscillatory total cross section as seen in Fig. 4(b). Though positions of the peaks and troughs in Fig. 5(a) are almost fully out of step, both plots have comparable amplitudes.

To see how they lead to very different total cross sections these terms must be coupled with the scattering matrix amplitude for the incident electron. For $\mathbf{H}'=\mathbf{G}'=\mathbf{H}=\mathbf{G}=\mathbf{0}$, the relevant term in Eq. (17) is $|\mathcal{S}_{\mathbf{0},\mathbf{0}}(\mathbf{K}_\perp=\mathbf{0},z)|^2|\mathcal{S}_{\mathbf{0},\mathbf{0}}(\mathbf{K}_\perp=\mathbf{0},t-z)|^2$, which is plotted in Fig. 5(b). The difference between the two thicknesses is now pronounced, the integrated contribution for $t=1150$ Å being twice as large as that for $t=1050$ Å. This follows because the peaks in Fig. 5(a) for the greater thickness coincide with those in the incident electron amplitude $|\mathcal{S}_{\mathbf{0},\mathbf{0}}(\mathbf{K}_\perp=\mathbf{0},z)|^2$, as seen in Fig. 3(c). Thus cases where the maxima in the oscillatory channeling amplitude of the incident electron coincide with those of the scattered electron lead to large total cross sections. Thicknesses at which the maxima of one tend to coincide with the minima of the other lead to smaller total cross sections. The result is that the channeling of both incident and scattered electrons conspire to give strong oscillatory behavior of the total cross section as a function of thickness.

C. Thickness averaging and comparison with experiment

The strong oscillatory behavior in the double-channeling cross section complicates the process of matching to experiment since several different thickness values can give quantitatively similar positioning and weighting of the peaks.

In the ideal world, one would prefer to compare calculations to data measured from a specimen of precisely known thickness. For the case of the NiO crystal employed during these measurements, we were not afforded this luxury. The single crystal of NiO used in this work, as described in Sec. II, was tapered in profile as would be the case of any specimen prepared by ion-beam milling. The wedge-shaped nature of the analyzed volume defined by the probe diameter varied from a minimum of around 39 nm to a maximum of around 78 nm. This deviation corresponds to the experimental observation that the outer periphery of the probe diameter was bounded at its thickness extremes by extinction contours corresponding to one and two extinction distances $\xi_{\mathbf{G}}$ for a $\langle 200\rangle$ reflection. We shall use this information as a constraint in a numerical fit to the data to estimate t and Δt where a sample with uniform thickness variation between thicknesses t and $t+\Delta t$ is assumed.

The experimental data was processed as follows. The centroid of the central peak for the experimental data was slightly offset, the digital step not being in perfect alignment with the center of the (000) beam. This was corrected by interpolation between the existing data points and shifting back to a symmetric position. In principle, for a perfect, slablike NiO crystal, the cross section for positive and negative tilts would be identical. This was not quite true of the experimental data and an average of the left and right halves was performed to generate a reduced data set. The variation of the halves about this average may be regarded as indicative of nonstatistical errors (specimen nonuniformity, electronic noise in the detector) and was taken as a rough estimate of the error in the data.

That said, it should be noted that some "error" will be introduced into the simulations through the approximations made. We simulate a systematic row orientation as an effective one dimensional problem, though this approximation cannot quite be realized in practice. We allow for an attenuation due to thermal scattering, but we do not include a diffuse contribution to account for detectable ionization events caused by thermally scattered electrons.

We define a fit parameter $f(t,\Delta t)$ which is simply a sum of squares measure,

$$f(t,\Delta t)=\sum_i [I_i^{\mathrm{expt}}(t,\Delta t)-a(t,\Delta t)I_i^{\mathrm{sim}}(t,\Delta t)]^2, \qquad (19)$$

where I^{expt} denotes the experimental number of counts, I^{sim} denotes the simulated number of counts, and the sum over i runs over the orientations in the (reduced) data set. The simulated intensity $I^{\mathrm{sim}}(t,\Delta t)$ is rescaled by a constant $a(t,\Delta t)$ for each different set of parameters $(t,\Delta t)$ such that the mean of the experimental and simulated data are the same. Some such pinning is necessary in a comparison with experimental data to put the number of counts on the same scale.

Figure 6(a) shows a surface plot of $f(t,\Delta t)$. This plot too shows oscillatory behavior. In particular, for small values of Δt there are values of t for which simulations are significantly different to experiment. At these points we tend to find significant differences either in the precise location of the Bragg peaks or, more usually, significant differences in the relative peak heights when comparing the simulations with the experimental data.

Figure 6(b) shows a contour plot of the fit parameter in Fig. 6(a) where the vertical range has been truncated to bring out the structure near the minima. The three significant minima evident have been labeled, with lower labels corresponding to deeper minima, and correspond to the $(t,\Delta t)$ parameter sets (1) (230 Å, 110 Å), (2) (450 Å, 120 Å), and (3) (685 Å, 110 Å). The lowest minimum occurs for a thickness range that is smaller than the lower bound on the thickness that was determined by experimental measurements. It can therefore be discarded. The second minimum is well within the likely range determined experimentally. The third

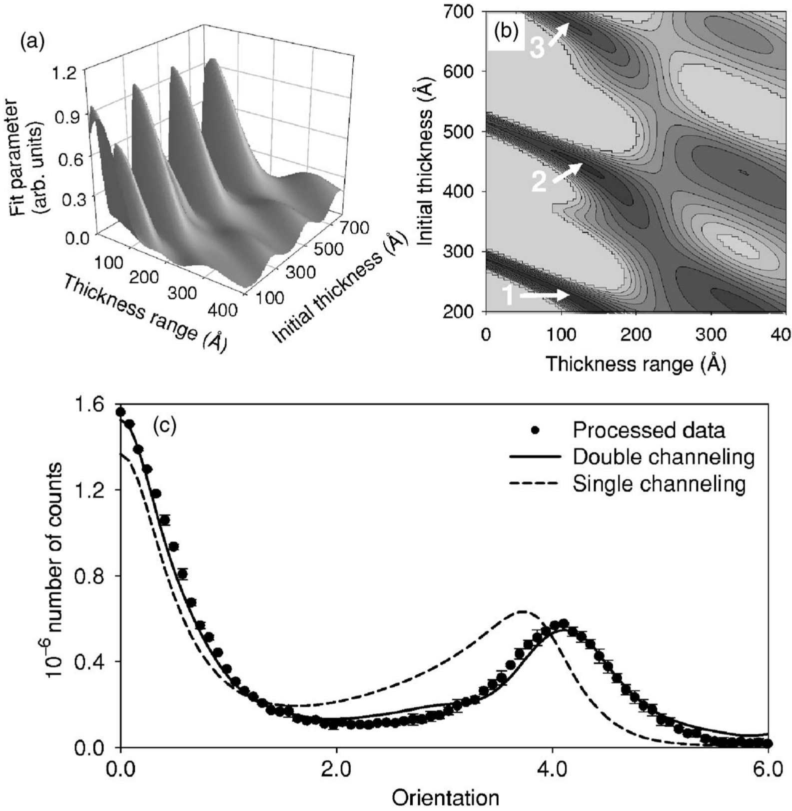

FIG. 6. (a) Fit parameter as a function of the initial thickness t and the thickness range Δt. (b) Contour plot of the fit parameter in (a) truncated to bring out the structure near the minima. Three significant minima, labeled by the white indices, are evident. The minima correspond to $(t,\Delta t)$ parameters (1) (230 Å, 110 Å), (2) (450 Å, 120 Å), and (3) (685 Å, 110 Å). (c) Comparison between the processed experimental data, the best-fit double-channeling simulation using the parameters from minimum 2, and the single-channeling simulation using the same parameters.

is also a possibility, though not so low a minimum as the second [the ratio of $f(t,\Delta t)$ values is 2.4, although this is not evident in Fig. 6(b) due to binning in the contour plot]. Therefore we estimate the the crystal thickness in the illuminated region varied between 450 and and 570 Å.

Figure 6(c) shows the processed data set, with error bars determined from the averaging procedure. The solid line shows the double-channeling simulation for the optimum parameters as determined by the fit, while the dashed line shows the single-channeling simulation for the same parameters. The double-channeling simulation agrees very well with the experimental data on the position and relative heights of the peaks. The same cannot be said of the single-channeling simulation, an indication that this is indeed a case where the double-channeling model is required to adequately model the experiment. There are some discrepancies between the double-channeling simulation and the experimental data between the peaks, but they are of less concern, within the expectations of the approximations made. It is clear that double-channeling is critical not just to obtain a good fit to the data but even to adequately predict the peak positions and relative intensities.

VI. CONCLUSION

We have presented the theory to describe electron energy loss cross sections in both single- and double-channeling models, incorporating the nonlocality of the effective scattering potential. The former, simpler case allowed us to introduce the Bloch wave and scattering theory methods while providing some insight about the origin of the Bragg peaks.

However, the more important consideration arising from the use of detectors with small acceptance angles is the necessity to include the channeling of the scattered electron, the double-channeling method. Using NiO as a case study, it was demonstrated that the double-channeling cross section oscillates significantly as a function of specimen thickness. As we have shown, this oscillatory behavior is a natural consequence of the channeling of the scattered electrons. The oscillatory behavior may complicate the use of simulations to set up or interpret experimental results if the specimen thickness is not well known, though in this case a fit to the data returned a plausible estimate for the thickness. The use of detectors with very small apertures aids approximations that increase the efficiency of the double-channeling calculations, facilitating further exploratory simulation.

Averaging over a range of energy losses enabled us to focus on the channeling effects rather than the fine structure. But an important consequence of these findings is the awareness that the optimum conditions for high-angular-resolution energy loss spectroscopy are precisely those for which the effects of channeling of the scattered electron are most pronounced.

ACKNOWLEDGMENTS

L.J.A. acknowledges support by the Australian Research Council. M.P.O. was supported by the Laboratory Directed Research and Development Program of ORNL, managed by UT-Battelle, LLC, for the U.S. Department of Energy under Contract No. DEAC05-00OR22725 and by ORNL. N.J.Z. was supported by the U.S. DoE BES under Contract No. MS W-31-109-Eng-38 at ANL.

[1] R. D. Leapman, P. L. Fejes, and J. Silcox, Phys. Rev. B **28**, 2361 (1983).

[2] Y. Y. Wang, S. C. Cheng, V. P. Dravid, and F. C. Zhang, Ultramicroscopy **59**, 109 (1995).

[3] Y.-Y. Wang, G. Feng, and A. L. Ritter, Phys. Rev. B **42**, 420 (1990).

[4] K. Lie, R. Brydson, and H. Davock, Phys. Rev. B **59**, 5361 (1999).

[5] N. J. Zaluzec, Microsc. Microanal. **6**, S2, 938 (2000).

[6] N. Jiang, B. Jiang, J. C. H. Spence, R. C. Yu, S. C. Li, and C. Q. Jin, Phys. Rev. B **66**, 172502 (2002).

[7] A. G. Marinopoulos, L. Reining, V. Olevano, A. Rubio, T. Pichler, X. Liu, M. Knupfer, and J. Fink, Phys. Rev. Lett. **89**, 076402 (2002).

[8] G. Radtke, T. Epicier, P. Bayle-Guillemaud, and J. C. L. Bossé, J. Microsc. **210**, 60 (2003).

[9] S. Lazar, G. A. Botton, M.-Y. Wu, F. D. Tichelaar, and H. W. Zandbergen, Ultramicroscopy **96**, 535 (2003).

[10] S. Lazar, C. Hébert, and H. W. Zandbergen, Ultramicroscopy **98**, 249 (2004).

[11] N. J. Zaluzec, M. G. Blackford, K. L. Smith, and M. Colella, Microsc. Microanal. **11**, S2, 718 (2005).

[12] L. J. Allen, S. D. Findlay, M. P. Oxley, C. Witte, and N. J. Zaluzec (unpublished).

[13] A. Howie, Proc. R. Soc. London, Ser. A **271**, 268 (1963).

[14] V. W. Maslen and C. J. Rossouw, Philos. Mag. A **49**, 735 (1984).

[15] C. J. Rossouw and V. W. Maslen, Philos. Mag. A **49**, 743 (1984).

[16] D. K. Saldin and P. Rez, Philos. Mag. B **55**, 481 (1987).

[17] D. M. Bird and A. G. Wright, Acta Crystallogr., Sect. A: Found. Crystallogr. **A45**, 104 (1989).

[18] S. L. Dudarev, L.-M. Peng, and M. J. Whelan, Phys. Rev. B **48**, 13408 (1993).

[19] P. Schattschneider, M. Nelhiebel, M. Schenner, W. Grogger, and F. Hofer, J. Microsc. **183**, 18 (1996).

[20] T. W. Josefsson and L. J. Allen, Phys. Rev. B **53**, 2277 (1996).

[21] H. Kohl and H. Rose, Adv. Electron. Electron Phys. **65**, 173 (1985).

[22] L. J. Allen and T. W. Josefsson, Phys. Rev. B **52**, 3184 (1995).

[23] P. Schattschneider, M. Nelhiebel, H. Souchay, and B. Jouffrey, Micron **31**, 333 (2000).

[24] V. W. Maslen, J. Phys. B **16**, 2065 (1983).

[25] V. W. Maslen and C. J. Rossouw, Philos. Mag. A **47**, 119 (1983).

[26] C. J. Rossouw and V. W. Maslen, Ultramicroscopy **21**, 277 (1987).

[27] L. J. Allen and C. J. Rossouw, Phys. Rev. B **47**, 2446 (1993).

[28] M. P. Oxley and L. J. Allen, Phys. Rev. B **57**, 3273 (1998).

[29] M. Nelhiebel, N. Luchier, P. Schorsch, P. Schattschneider, and B. Jouffrey, Philos. Mag. B **79**, 941 (1999).

[30] C. Dwyer, Phys. Rev. B **72**, 144102 (2005).

[31] M. P. Oxley, E. C. Cosgriff, and L. J. Allen, Phys. Rev. Lett. **94**, 203906 (2005).

[32] N. J. Zaluzec, B. J. Kestel, and D. Henriks, Microsc. Microanal. **3**, S2, 983 (1997).

[33] N. J. Zaluzec, in *Encyclopedia of Materials Characterization*, edited by R. Brundle, C. Evans, and S. Wilson (Elsevier, Amsterdam, 1991), pp. 135–148.

[34] L. Van Hove, Phys. Rev. **95**, 249 (1954).

[35] E. C. Cosgriff, M. P. Oxley, L. J. Allen, and S. J. Pennycook, Ultramicroscopy **102**, 317 (2005).

[36] R. F. Egerton, *Electron Energy-Loss Spectroscopy in the Electron Microscope*, 2nd ed. (Plenum Press, New York, 1996).

[37] W. Coene and D. Van Dyck, Ultramicroscopy **33**, 261 (1990).

[38] L. J. Allen, S. D. Findlay, M. P. Oxley, and C. J. Rossouw, Ultramicroscopy **96**, 47 (2003).

[39] L. J. Allen, Ultramicroscopy **48**, 97 (1993).